




Moving media as photonic heat engine and pumpYoichiro Tsurimaki , Renwen Yu , and Shanhui Fan **Department of Electrical Engineering, Ginzton Laboratory, Stanford University, Stanford, California 94305, USA*

(Received 9 November 2022; revised 15 February 2023; accepted 16 February 2023; published 7 March 2023)

A system consisting of two slabs with different temperatures can exhibit a nonequilibrium lateral Casimir force on either one of the slabs when Lorentz reciprocity is broken in at least one of the slabs. This system constitutes a photonic heat engine that converts radiative heat into work done by the nonequilibrium lateral Casimir force. Reversely, by sliding two slabs at a sufficiently high relative velocity, heat is pumped from the slab at a lower temperature to the other one at a higher temperature. Hence the system operates as a photonic heat pump. In this paper, we study the thermodynamic performance of such a photonic heat engine and pump via the fluctuational electrodynamics formalism. The propulsion force due to the nonreciprocity and the drag force due to the Doppler effect were revealed as the physical mechanisms behind the heat engine. We also show that in the case of the heat pump, the use of nonreciprocal materials can help reduce the required velocity. We present an ideal material dispersion to reach the Carnot efficiency limit. Furthermore, we derive a relativistic version of the thermodynamic efficiency for our heat engine and prove that it is bounded by the Carnot efficiency that is independent of the frame of reference. Our paper serves as a conceptual guide for the realization of photonic heat engines based on fluctuating electromagnetic fields and relativistic thermodynamics and shows the important role of electromagnetic nonreciprocity in operating them.

DOI: [10.1103/PhysRevB.107.115406](https://doi.org/10.1103/PhysRevB.107.115406)**I. INTRODUCTION**

The effects of radiative heat transfer and nonequilibrium Casimir force can both occur between two objects having different temperatures, due to the exchange of energy and momentum as carried by thermally fluctuating electromagnetic fields emitted from the objects. The significant enhancement of these effects [1–20], when the two objects are brought in close proximity separated by nanoscale gaps, has motivated extensive studies due to the fundamental importance of these effects as well as opportunities for energy [21–25] and optomechanical applications at nanoscales [26–29]. The focus of most of these studies was on either radiative heat transfer or Casimir force alone. On the other hand, since both effects arise from the same underlying thermal electromagnetic fields, it should be of interest to study the relationship and the conversion between radiative heat transfer and nonequilibrium Casimir forces.

Recently, it was shown that materials with different temperatures can experience nonequilibrium Casimir force in the direction parallel to the interacting surfaces when at least one of them breaks Lorentz reciprocity, i.e., when at least one of them is made of nonreciprocal materials [30–37]. While lateral Casimir force can also exist in reciprocal systems both at thermal equilibrium [27,28,38–41] and nonequilibrium [42,43], the objects must break translational or rotational symmetry. Moreover, the lateral force in reciprocal systems both in thermal equilibrium and nonequilibrium results in a relaxation process to mechanical equilibrium, and contin-

uous external stimuli such as external illumination of light or mechanical work are necessary to realize the persistent lateral force. In contrast, breaking Lorentz reciprocity of the system allows persistent nonequilibrium lateral Casimir force on translationally or rotationally invariant objects so far as the objects are in thermal nonequilibrium.

This existence of such a persistent lateral force suggests the possibility of a heat engine that converts the radiative heat transfer into mechanical work done by nonequilibrium lateral Casimir force. Recently, a single gyrotropic sphere at a different temperature from the environment was analyzed as a heat engine where the radiative heat transfer between the sphere and the environment results in the mechanical torque on the sphere [36]. The thermodynamic analysis revealed that the thermodynamic efficiency is bounded by the Carnot efficiency limit and magnetic hyperbolic plasma was proposed as a material that can be used to approach the Carnot limit in this system. The nonequilibrium lateral Casimir force in a parallel plate configuration has also been explored for the construction of a heat engine [37]. The parallel plate geometry is desirable since it allows for the possibility of scaling up such a heat engine. The analysis in [37] however was based on the linear order approximation of radiative heat transfer and nonequilibrium lateral Casimir force [44] with respect to the velocity and temperature difference. The validity of such linear approximation is limited to small temperature differences as well as small velocities of relative motion. To our best knowledge, the detailed analysis of two semi-infinite parallel slabs at relative motion as a heat engine has not been performed. Moreover, the reverse process, i.e., operation as a heat pump, was not analyzed before due to the requirement

*shanhui@stanford.edu

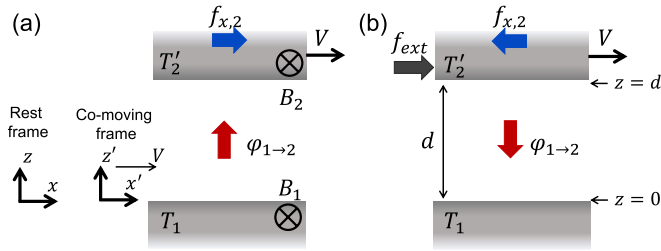


FIG. 1. Two semi-infinite parallel slabs separated by a vacuum gap d that are moving relative to each other at constant velocity V along the x direction. Two slabs are at the proper temperatures T_1 and T_2' in the rest and comoving frames, respectively. The physical quantities with the prime mark are defined in the comoving frame. (a) The system operating as a heat engine where the net heat flux $\varphi_{1\rightarrow 2}$ from slab 1 to slab 2 is converted into work driven by nonequilibrium lateral Casimir force $f_{x,2}$ on slab 2 under proper directions of external magnetic fields. (b) The system operating as a heat pump where the external work done by the force f_{ext} pumps heat from slab 2 at a low proper temperature to slab 1 at a higher proper temperature. External magnetic fields are not necessary.

of high velocities of relative motion, which is beyond the applicability of the linear approximation.

In this paper, we analyze a system consisting of two semi-infinite parallel slabs in thermal nonequilibrium as a photonic heat engine as well as a photonic heat pump. The photonic heat engine [Fig. 1(a)] operates by the conversion of radiative heat flux from a high-temperature to a low-temperature slab into relative motion between the slabs driven by nonequilibrium lateral Casimir force. We show that the same system operates as a photonic heat pump [Fig. 1(b)] where the radiative heat flows from the low-temperature to the high-temperature slab at high velocities of relative motion driven by external work. We reveal that nonreciprocity and Doppler effects play essential roles in the operation of the heat engine and pump. Compared to the previous work [37], we analyze the operation of the heat engine at different velocities of relative motion from the rest to the steady-state velocity. For the heat engine, nonreciprocity allows the heat engine to self-start and the Doppler effect makes the heat engine reach the steady-state velocity. We show that the same system as the heat engine operates as a photonic heat pump at high velocities of relative motion realized by external work. Such a heat pump was suggested but not considered in detail in previous works [36,37]. For the heat pump, breaking material's reciprocity is not necessary since nonreciprocal wave propagations can be induced by the relative motion. However, the use of nonreciprocal materials allows the operation of the heat pump at lower relative velocities and enhances the performance of the heat pump. Furthermore, the operation of the heat pump at nonrelativistic velocities requires the slabs to be in the near field. We also show that the photonic heat engine can achieve Carnot efficiency and derive an ideal dispersion of materials that approach the Carnot limit. In principle, we can conceive of operating the heat engine and pump at relativistic velocities. For such situations, we derive the relativistic thermodynamic efficiency and show that it is bounded by the Carnot efficiency that is independent of the frame of reference.

The paper is organized as follows. In Sec. II, we derive the fluctuational electrodynamics formalism of radiative heat transfer and lateral Casimir force between two semi-infinite slabs at a relative motion separated by a vacuum gap. The formalism is applicable to nonmagnetic slabs with general dielectric function tensors at a relative motion with arbitrary velocities. We also discuss the constraints related to the second law of thermodynamics and imposed by Lorentz reciprocity. In Secs. III and IV, we analyze the system as a heat engine and a heat pump, respectively. In Sec. V, we derive the relativistic thermodynamic efficiency of our heat engine. In Sec. VI, we summarize our findings.

II. FORMALISM

We consider two semi-infinite parallel slabs labeled as 1 and 2 that are separated by a vacuum gap d as shown in Fig. 1. Two slabs can move laterally at a constant velocity V . We derive the radiative heat flux and lateral Casimir force per unit surface area, i.e., shear stress, between the two slabs in relative motion in the framework of fluctuational electrodynamics [45]. Previous studies have investigated radiative heat transfer between two slabs with general dielectric function tensors at rest [46,47], shear stress on two slabs of isotropic media in a relative motion [48,49], and the friction coefficient, i.e., the ratio of the shear stress to the velocity of relative motion, in the linear response regime between two slabs of anisotropic materials [37]. As a step further, in this paper we develop the fluctuational electrodynamic formalism for radiative heat flux and shear stress between two slabs with general dielectric function tensors in relative motion at arbitrary velocity. This formalism is applicable to materials breaking Lorentz reciprocity. Our development is motivated by the observation that in the two-slab system, one of the slabs must be nonreciprocal in order to construct a heat engine driven by the nonequilibrium lateral Casimir force [36,37]. Moreover, to have a complete picture of the operation of such a heat engine, it is important to go beyond the linear response regime. In this section, we describe the main results of our formalism. A detailed derivation can be found in Supplemental Material (SM) [50] (see also [51] therein).

Due to quantum and thermal fluctuations, any object made of lossy materials emits electromagnetic waves. Radiative heat transfer and Casimir force between the slabs occur by such emission from one slab and the absorption by the other slab. The absorption and emission processes, moreover, involve multiple reflections of the waves between the slabs. The strength of the fluctuations, as well as the absorption and emission processes, depend on the temperatures and optical properties of the slabs. Since the physical properties of a slab are well defined in its rest frame where the local thermodynamic equilibrium is established, we incorporate the effects of the relative motion between the slabs by the Lorentz transformation of the electromagnetic waves in the vacuum between the slabs. Thus, we need not perform the Lorentz transformation of thermodynamic quantities.

In this paper, we assume that slab 1 is at rest whereas slab 2 can move, and we refer to the frames in which slabs 1 and 2 are at rest as the rest frame and the comoving frame, respectively. We use primes on the physical quantities in the comoving

frame. We consider the two slabs at the proper temperatures T_1 and T_2' , respectively. We assume the slabs are made of linear and nonmagnetic materials, i.e., the relative magnetic permeability is unity. Under the framework of fluctuational electrodynamics with these assumptions, our formalism is exact. Without loss of generality, we also assume slab 2 is moving at the velocity V in the x direction with respect to slab 1. For the observer in the rest frame, the net radiative heat flux $\varphi_{1\rightarrow 2}$ from slab 1 to slab 2 and the net shear stress $f_{x,1}$ on slab 1 are given as

$$\begin{bmatrix} \varphi_{1\rightarrow 2} \\ f_{x,1} \end{bmatrix} = \int_0^\infty \frac{d\omega}{2\pi} \int \frac{d\mathbf{q}}{(2\pi)^2} \begin{bmatrix} \hbar\omega \\ -\hbar q_x \end{bmatrix} \times [n_B(\omega, T_1) - n_B(\omega', T_2')] \tau_{1\rightarrow 2}(\omega, \mathbf{q}; V), \quad (1)$$

where ω and $\mathbf{q} = (q_x, q_y)$ are the angular frequency and the in-plane wave-vector components of the electromagnetic waves, $n_B(\omega, T) = \frac{1}{\exp(\frac{\hbar\omega}{k_B T}) - 1}$ is the Bose-Einstein distribution, and \hbar and k_B are the reduced Planck constant and the Boltzmann constant, respectively. The shear stress on slab 2 is related as $f_{x,2} = -f_{x,1}$. $\tau_{1\rightarrow 2}$ is the transmission coefficient for the electromagnetic waves emitted from slab 1 and absorbed by slab 2. For the propagative waves ($q = |\mathbf{q}| < k_0 = \frac{\omega}{c}$) and evanescent waves ($q > k_0$), the transmission coefficients are given as

$$\tau_{1\rightarrow 2}(\omega, \mathbf{q}; V) = \begin{cases} \text{Tr} \left[(I - \tilde{R}_2^\dagger \tilde{R}_2) \frac{1}{D_{12}} (I - R_1 R_1^\dagger) \frac{1}{D_{12}^\dagger} \right], & q < k_0 \\ \text{Tr} \left[(\tilde{R}_2^\dagger - \tilde{R}_2) \frac{1}{D_{12}} (R_1 - R_1^\dagger) \frac{1}{D_{12}^\dagger} e^{-2\kappa_z d} \right] & q > k_0 \end{cases}, \quad (2)$$

where I is the 2×2 identity matrix, $D_{12} = I - R_1 \tilde{R}_2 e^{2ik_z d}$, k_z is the z component of the wave vector in the vacuum, $\kappa_z = \sqrt{q^2 - k_0^2}$, and $\tilde{R}_2 = LR_2'(L^T)^{-1}$. R_1 and R_2' are the reflection matrices of slabs 1 and 2 in the linear polarization basis, respectively, and their explicit expressions are

$$R_1 = \begin{bmatrix} r_1^{ss}(\omega, \mathbf{q}) & r_1^{sp}(\omega, \mathbf{q}) \\ r_1^{ps}(\omega, \mathbf{q}) & r_1^{pp}(\omega, \mathbf{q}) \end{bmatrix}, \quad (3)$$

$$R_2' = \begin{bmatrix} r_2^{ss}(\omega', \mathbf{q}') & r_2^{sp}(\omega', \mathbf{q}') \\ r_2^{ps}(\omega', \mathbf{q}') & r_2^{pp}(\omega', \mathbf{q}') \end{bmatrix},$$

where r_k^{ij} ($i, j = s, p$ and $k = 1, 2$) is the Fresnel reflection coefficient for the j -polarized incident light and the i -polarized reflected light for slab k . Note that the reflection matrix of slab 2, R_2' , is evaluated in the comoving frame. The angular frequency and wave vector in the two frames are related by the Lorentz transformation as

$$\omega' = \gamma(\omega - q_x V), \quad q'_x = \gamma(q_x - \beta k_0), \quad q'_y = q_y, \quad k'_z = k_z, \quad (4)$$

where $\beta = \frac{V}{c}$ and $\gamma^{-1} = \sqrt{1 - \beta^2}$.

The matrix L transforms the electric fields of forward propagating waves in the vacuum, i.e., the waves propagating towards the positive z direction, from the rest frame to the comoving frame via the Lorentz transformation. It is

expressed as

$$L = \frac{k'_0 \gamma}{k_0 q q'} \begin{bmatrix} q^2 - \beta k_0 q_x & \beta k_z q_y \\ -\beta k_z q_y & q^2 - \beta k_0 q_x \end{bmatrix}, \quad (5)$$

where $k'_0 = \frac{\omega'}{c}$ and $q' = |\mathbf{q}'|$. Similarly, L^T transforms backward propagating waves, and L^{-1} transforms the forward propagating waves from the comoving frame to the rest frame. Thus, from the viewpoint of the observer in the rest frame, the reflection of electromagnetic waves from the moving slab 2 is calculated by three steps as indicated in $\tilde{R}_2 = LR_2'(L^T)^{-1}$. First, the forward propagating waves are Lorentz transformed from the rest to the comoving frame by L , the reflection is calculated in the comoving frame by R_2' , and the backward propagating waves, represented by L^T , are transformed from the comoving frame to the rest frame by $(L^T)^{-1}$. We note that the inverse of L exists for all the electromagnetic modes that contribute to heat and momentum transfer (see discussions in SM [50]).

Two identities are imposed on the transmission coefficient $\tau_{1\rightarrow 2}$ in our formalism. Previously, for the case of two nonmagnetic slabs with general dielectric function tensors at rest, direct calculations showed the relation $\tau_{1\rightarrow 2}(\omega, \mathbf{q}) = \tau_{2\rightarrow 1}(\omega, \mathbf{q})$ [47]. This relation guarantees that the system satisfies the second law of thermodynamics [47], which requires that $\varphi_{1\rightarrow 2} = 0$ when $T_1 = T_2$ at $V = 0$. Moreover, the reflection matrix of a reciprocal material satisfies $R_i(\omega, -\mathbf{q}) = \sigma_z R_i^T(\omega, \mathbf{q}) \sigma_z$, where σ_z is the Pauli matrix. Therefore, if both slabs are made of reciprocal materials, the transmission coefficient is further constrained as $\tau_{1\rightarrow 2}(\omega, \mathbf{q}) = \tau_{1\rightarrow 2}(\omega, -\mathbf{q})$ [47]. We extend these results for the case of two nonmagnetic slabs with general dielectric function tensors at relative motion. When the slabs are in relative motion, direct calculations show

$$\tau_{1\rightarrow 2}(\omega, \mathbf{q}; V) = \tau_{2\rightarrow 1}(\omega, \mathbf{q}; V). \quad (6)$$

If the two slabs are made of reciprocal materials, the constraint on the transmission coefficient is derived as

$$\tau_{1\rightarrow 2}(\omega, -\mathbf{q}; V) = \tau_{1\rightarrow 2}(\omega, \mathbf{q}; -V), \quad (7)$$

where $-V$ on the right-hand side means that object 2 is moving towards the negative x direction. Equation (7) indicates that the propagation of electromagnetic waves becomes nonreciprocal in the presence of relative motion even when the materials are reciprocal in the respective rest frames. The nonreciprocal propagation induced by moving materials was previously discussed in many different contexts such as the Fizeau drag [52], and the acoustic and optical wave isolation [53,54].

Radiative heat flux and shear stress are not Lorentz scalars. With respect to the Lorentz transformation, the frequency and momentum form a four-vector $q^\mu = (\omega/c, q_x, q_y, k_z)$, whereas the electromagnetic fields form a tensor. From Eq. (1), therefore, the radiative heat flux and shear stress also form a four-vector $f^\mu = (-\frac{\varphi_{1\rightarrow 2}}{c}, f_{x,1}, f_{y,1}, f_{z,1})$ as far as the Lorentz boost within the xy plane is concerned. The four-vector transforms between the rest and comoving frame via $f'^\mu = \Lambda^\mu_\nu f^\nu$ where Λ^μ_ν is the Lorentz boost along the xy plane (see SM [50] for details). Thus, the radiative heat flux and shear stress between the two frames in our system are

related as

$$\varphi'_{1\rightarrow 2} = \gamma(\varphi_{1\rightarrow 2} + f_{x,1}V), \quad (8)$$

where $\varphi'_{1\rightarrow 2}$ is the radiative heat flux from slab 1 to slab 2 for the observer in the comoving frame. We also obtained Eq. (8) by direct calculations.

Finally, the thermodynamic efficiency of our heat engine η and the coefficient of performance (COP) of our heat pump are defined for $T_1 > T_2'$ as

$$\eta = \frac{f_{x,2}V}{\varphi_{1\rightarrow 2}}, \quad \text{COP} = \frac{\varphi_{1\rightarrow 2}}{f_{x,2}V}, \quad (9)$$

where this efficiency η and COP are meaningful only for $f_{x,2}V > 0$ and $\varphi_{1\rightarrow 2} < 0$, respectively. We also note that the definition in Eq. (9) is sensible for nonrelativistic velocities, i.e., $\frac{V}{c} \ll 1$, and we discuss the relativistic corrections in Sec. V.

III. HEAT ENGINE

Using the formalism as described in the previous section, we analyze the two-slab structure as schematically shown in Fig. 1(a) from the perspective of using it as a heat engine. This heat engine converts the radiative heat flux into mechanical work driven by the nonequilibrium lateral Casimir force. Practically, a heat engine should be able to self-start. Thus, the two-slab system needs to support a lateral force at $V = 0$ when both slabs are at rest. To fulfill this requirement, two conditions need to be satisfied as can be obtained by examining Eq. (1). First, the two slabs must have different temperatures. For this two-slab system, in general, the radiative heat flux and the shear stress will be identically zero if the slabs are in thermal equilibrium with each other. Second, at least one of the slabs must contain nonreciprocal materials. If both slabs are made entirely of reciprocal materials, the momentum transfer at \mathbf{q} and $-\mathbf{q}$ cancels out, resulting in null lateral force. This can be seen by observing that the integrand in Eq. (1) for $f_{x,1}$ is an odd function of q_x , since the transmission coefficient satisfies the condition $\tau_{1\rightarrow 2}(\omega, -\mathbf{q}; V = 0) = \tau_{1\rightarrow 2}(\omega, \mathbf{q}; V = 0)$ from Eq. (7). These two requirements were also discussed in previous works [36,37].

Based on the discussion above, we consider an n -doped indium antimonide (n -InSb), a well-known magneto-optical material, as the slab material. To break the reciprocity, we externally apply static magnetic fields in the y direction on the two slabs as shown in Fig. 1(a). The direction of the external magnetic fields is selected to be perpendicular to the intended direction of motion of the slabs along the x direction, so that the degree of asymmetry in the wave propagations will be the greatest and the resulting nonequilibrium lateral force in the x direction will be the largest. In this paper, we assume that the external static magnetic fields on slabs 1 and 2 are independently applied in the rest frame and the comoving frame, respectively. If the external magnetic field is applied on both slabs in the rest frame, the external field on the moving slab in the comoving frame is composed of static magnetic and electric fields, i.e., $B'_y = \gamma B_y$, and $E'_z = \gamma V B_y$ where B_y is an external static magnetic field in the rest frame, which complicates our theoretical treatment. As long as we consider the heat engine and pump operating at nonrelativistic velocities,

i.e., $\gamma = 1$ and $V \ll c$, the two ways of applying the external static magnetic fields give approximately the same results.

Under an external static magnetic field in the positive y direction, the dielectric function of n -InSb is given as

$$\frac{\varepsilon(\omega)}{\varepsilon_\infty} = I_3 + \varepsilon_{\text{ph}}I_3 - \frac{\omega_p^2}{(\omega + i\gamma)^2 - \omega_c^2} \times \begin{bmatrix} 1 + i\frac{\gamma}{\omega} & 0 & -\frac{i\omega_c}{\omega} \\ 0 & \frac{(\omega+i\gamma)^2 - \omega_c^2}{\omega(\omega+i\gamma)} & 0 \\ \frac{i\omega_c}{\omega} & 0 & 1 + i\frac{\gamma}{\omega} \end{bmatrix}, \quad (10)$$

where I_3 is the 3×3 identity matrix, $\omega_p = \sqrt{n_e e^2 / (m_{\text{eff}} \varepsilon_0 \varepsilon_\infty)}$ is the plasma frequency, $\gamma = 3.39 \times 10^{12}$ rad/s is the electron scattering rate, and $\omega_c = eB/m_{\text{eff}}$ is the cyclotron frequency. The carrier concentration and the electron effective mass are taken to be $n_e = 1.07 \times 10^{17}$ cm $^{-3}$ and $m_{\text{eff}} = 0.022m_e$ where m_e is the bare electron mass, respectively. The bound electron and ions contribution to the dielectric function is incorporated in $\varepsilon_\infty = 15.7$. The phonon contribution ε_{ph} is given by the Lorenz model as

$$\varepsilon_{\text{ph}}(\omega) = \frac{\omega_L^2 - \omega_T^2}{\omega_T^2 - \omega^2 - i\Gamma\omega}, \quad (11)$$

where $\omega_L = 3.62 \times 10^{13}$ rad/s, $\omega_T = 3.39 \times 10^{13}$ rad/s, and $\Gamma = 5.65 \times 10^{11}$ rad/s. All the parameters in the model of n -InSb above are taken from [55,56].

Figure 2 shows the performance of the heat engine. We set the temperatures of the slabs to be $T_1 = 305$ K and $T_2' = 300$ K, respectively, and the separation between the slabs to be $d = 10$ nm throughout this paper. Note that the small gap between the slabs is not required for the operation as a heat engine, but rather is selected to enhance the power output. In our system, the coupled surface plasmon modes, as well as phonon-polariton modes, have large in-plane momenta as compared with the maximal in-plane momentum of free-space photons at the frequency, i.e., $q_x \gg k_0$, which contributes to larger lateral forces.

Figure 2(a) shows the radiative heat flux from slab 1 to slab 2 as a function of the velocity of relative motion under different magnitudes of the magnetic fields. For two slabs under antiparallel static magnetic fields, at a fixed velocity, the radiative heat flux decreases as the magnetic field increases in the considered range. The reduction of the radiative heat flux at increasing velocities is due to Doppler shift, and is further related to the interplay of the evolution of surface plasmon and phonon-polariton waves, as well as hyperbolic modes that progressively appear as the magnetic field increases [55]. All these aspects will be discussed in detail later. Practically, it is challenging to apply antiparallel static magnetic fields for two slabs separated by a nanoscale gap. Therefore, we also consider applying an external static magnetic field to only one of the slabs, i.e., $B_1 = 0$ T and $B_2 = -3$ T. The results, shown in the green curve in Fig. 2(a), have qualitatively the same behavior as the cases when antiparallel magnetic fields are applied to the two slabs. We also note that the shear force is zero at $V = 0$ when the same magnetic fields are applied to both slabs (not shown in Fig. 2). This is consistent with the observation of the symmetry in heat flux spectra when the same magnetic field is applied [47].

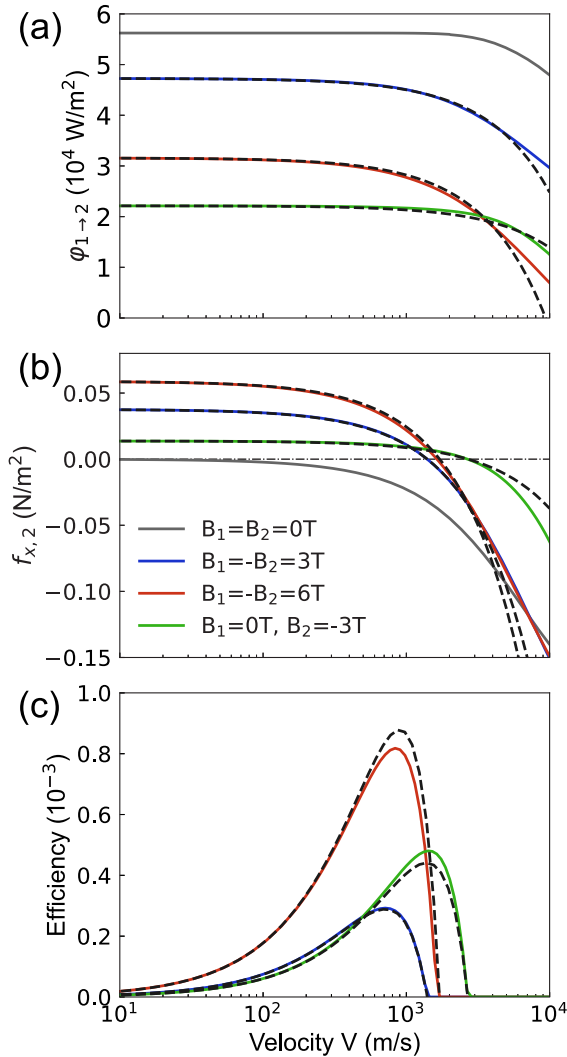


FIG. 2. (a) Radiative heat flux from slab 1 to slab 2, (b) shear stress on slab 2, and (c) thermodynamic efficiency of the heat engine as a function of the velocity of relative motion. Two slabs made of n -InSb are at $T_1 = 305$ K and $T_2' = 300$ K and separated by $d = 10$ nm. The results for different magnitudes of external magnetic fields are shown. The dash-dotted line in panel (b) describes $f_{x,2} = 0$. The results of the linear approximation Eqs. (12) and (14) are plotted in the dashed lines.

Figure 2(b) shows the shear stress on slab 2. In the absence of the external magnetic field, the shear stress is zero at rest, in consistency with the discussions above. For a moving object, a force that is along the direction of the velocity accelerates the motion of the object. We refer to such a force as a propulsion force. A force with a direction opposite to that of the velocity decelerates the motion of the object. We refer to such a force as a drag force. We also use these wordings of propulsion or drag forces to refer to the different components of a total force. When slab 2 moves in the positive x direction as a result of external mechanical work, the shear stress on slab 2 acts as a drag force, as previously shown for the isotropic materials [48]. This drag force is due mostly to the Doppler shift in the angular frequency. In contrast, in the presence of the external magnetic fields, the shear stress on slab 2 is

nonzero even at rest. Therefore, the shear stress here propels slab 2 in the positive x direction, allowing the heat engine to self-start, and acts as a propulsion force after slab 2 starts moving. Figure 2(b) shows that the shear stress on slab 2 at nonzero V acts as a propulsion force over a wide range of V . In this range, within the total shear stress, the propulsion force component is greater than the drag force component. As the velocity of slab 2 increases, the total force acting on slab 2 decreases due to the increasing drag force component and becomes zero at a steady-state velocity. Under the simulation condition, the steady-state velocity is around $V \approx 10^3$ m/s. This steady state is stable: further increase of the velocity results in the net drag force on slab 2. Therefore, to go beyond the steady-state velocity, external work must be applied, and the two-slab structure no longer operates as a heat engine.

We analyze the spectral contribution to the shear stress, i.e., the integrand of the ω integral in Eq. (1), to reveal the mechanism behind the velocity dependence of the radiative heat flux and shear stress. Figure 3(a) shows the spectral distribution of the shear stress on slab 2 for different velocities when the two slabs are under the antiparallel magnetic fields of 3 T. First, we discuss the origin of the three peaks and their signed contributions at $V = 0$ m/s. Since the system is translationally invariant and the in-plane momentum is conserved upon reflection, the momentum transfer between slabs can only occur through the emission and absorption processes. Therefore, the momentum transfer to slab 2 can arise either due to the absorption of the thermal emission from slab 1 or the emission of slab 2. Figure 3(b) shows the transmission coefficient τ at $V = 0$ m/s as a function of frequency ω and the in-plane wave-vector component along the x direction q_x . For other modes with nonzero q_x and q_y , the qualitative characteristics of the transmission coefficient are similar (see SM [50]). From Fig. 3(b), surface plasmon and surface phonon-polariton modes at around $\omega = 1.9 \times 10^{13}$ and 3.8×10^{13} rad/s, respectively, are supported at $q_x > 0$ but not at $q_x < 0$. When the two slabs are at rest, the number of emitted thermal photons from slab 1 is greater than that from slab 2, $n_B(\omega, T_1) > n_B(\omega, T_2')$. Thus, for these surface modes, the force on slab 2 due to the absorption of thermal radiation emitted by slab 1, which acts as a propulsion force, is greater than the recoil force on slab 2 due to its emission, which acts as a drag force. As a result, the contributions to the lateral force $f_{x,2}(\omega)$ from these two peaks are positive. Similarly, the negative spectral lateral force arises from the surface plasmon modes supported at around $\omega = 4.6 \times 10^{13}$ rad/s at $q_x < 0$.

We note that the lack of symmetry in $\tau(\omega, q_x)$, i.e., the fact that $\tau(\omega, q_x) \neq \tau(\omega, -q_x)$, is essential for the presence of lateral forces. The lateral forces would have been zero if $\tau(\omega, q_x) = \tau(\omega, -q_x)$. Thus, following an argument in [47], which states that for a reciprocal two-slab system $\tau(\omega, q_x) = \tau(\omega, -q_x)$ at $V = 0$, in reciprocal two-slab systems there is no lateral force at $V = 0$. We also note that the radiative heat flux is dominated by those surface modes and flows from slab 1 to slab 2 irrespective of the sign of q_x as shown in Fig. 3(d).

In Fig. 3(a), the magnitudes of the three peaks vary with respect to the velocity. Such variations primarily originate from the Doppler shift of the angular frequency, which affects the thermal photon occupation number for the emission from slab 2. The transmission coefficient τ has a negligible depen-

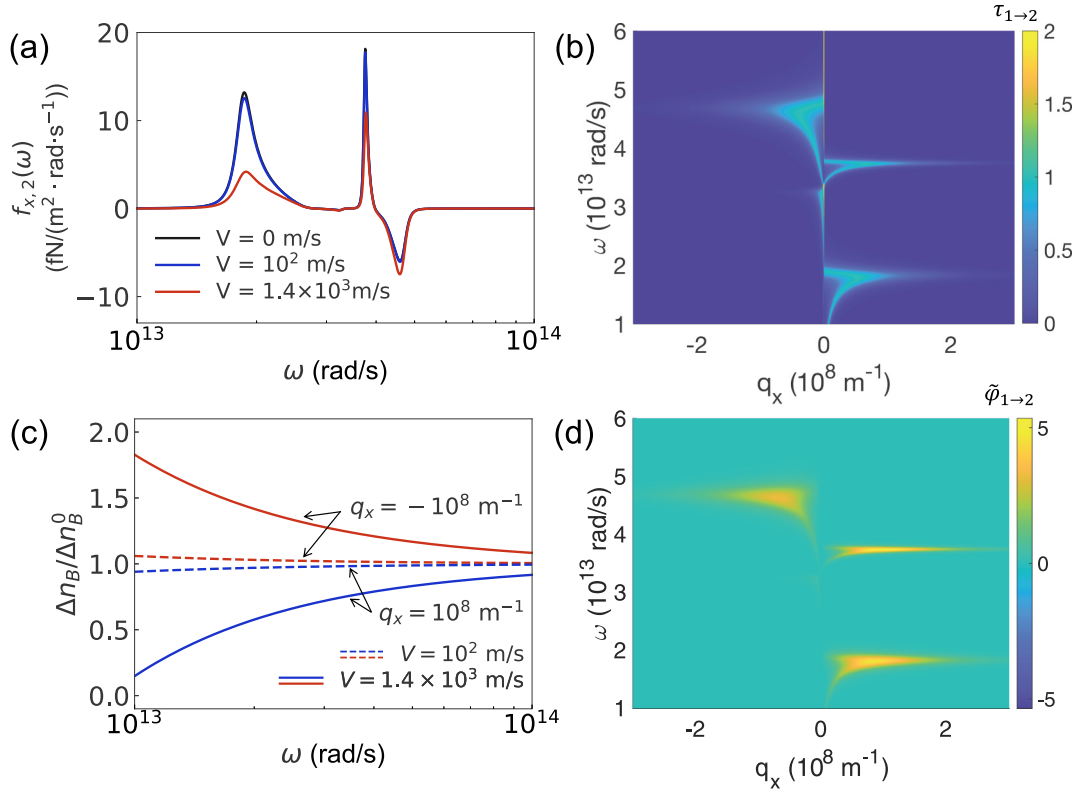


FIG. 3. (a) Spectral shear stress on slab 2 for different velocities of relative motion. (b) Plot of the transmission coefficient τ as a function of the frequency ω and x component of the wave vector q_x when two slabs are at rest. The transmission coefficient is plotted for the modes with in-plane wave vectors along the x direction, i.e., $\mathbf{q} = (q_x, 0)$. The magnetic fields are $B_1 = -B_2 = 3T$. (c) The ratio of the net transferred thermal photon number with relative motion $\Delta n_B = n_B(\omega, T_1) - n_B(\omega', T_2')$ to the one without relative motion $\Delta n_B^0 = n_B(\omega, T_1) - n_B(\omega, T_2')$ for fixed $q_x = \pm 10^8 \text{ m}^{-1}$ at $V = 10^2$ and $1.4 \times 10^3 \text{ m/s}$. (d) Plot of mode-resolved radiative heat flux $\tilde{\varphi}_{1 \rightarrow 2}(\omega, q_x, q_y)$ defined as $\varphi_{1 \rightarrow 2} = \int_0^\infty d\omega \int_{-\infty}^\infty dq \tilde{\varphi}_{1 \rightarrow 2}(\omega, q_x, q_y)$ for the same condition as panel (b). The unit is $[10^{-15} \frac{\text{W}\cdot\text{s}}{\text{rad}}]$. The other physical parameters are the same as those in Fig. 2.

dency on the velocity range of the heat engine (see SM [50]). Suppose that slab 2 is moving at a nonrelativistic velocity $V > 0$, i.e., $\gamma \approx 1$. In the rest frame, consider the thermal radiation emitted by slab 2 with $q_x > 0$ and ω . In the comoving frame, this thermal radiation has a frequency $\omega' = \omega - q_x V$, which is smaller than ω , and an in-plane momentum $q'_x = q_x - \beta k_0 \approx q_x$, where $\beta = V/c$. Thus, the frequency of the radiation is blue-shifted from the viewpoint of the observer in the rest frame. On the other hand, the number of photons does not change in the two frames and an observer in the rest frame sees the same number of thermally emitted photons as the observer in the comoving frame, which is given as $n_B(\omega', T_2')$. Thus, the frequency spectrum of the photon number flux that the observer in the rest frame sees is velocity dependent. For the waves with $q_x > 0$, the number of thermal photons at a frequency ω is exponentially enhanced at $V > 0$ compared to the number at $V = 0$, since $n_B(\omega', T_2') \approx e^{-\frac{\hbar\omega}{k_B T_2'}} e^{\frac{\hbar q_x V}{k_B T_2'}}$ for $\hbar(\omega - q_x V) \gg k_B T_2'$. As a result, as the velocity of slab 2 along the x direction increases, the emission of thermal photons with $q_x > 0$ from slab 2 is exponentially enhanced. This has the effect of enhancing the recoil force, which reduces the total force that propels slab 2. To illustrate this effect, Fig. 3(c) shows the ratio of the number of net transferred thermal photons per mode at a frequency ω in the presence

of relative motion, $\Delta n_B = n_B(\omega, T_1) - n_B(\omega', T_2')$, to the one without relative motion, $\Delta n_B^0 = n_B(\omega, T_1) - n_B(\omega, T_2')$. The plotted relative velocities are the same as those in Fig. 3(a) with in-plane wave vectors $q_x = \pm 10^8 \text{ m}^{-1}$, which has a typical magnitude. For the waves with $q_x > 0$, the net transferred thermal photon number from slab 1 to slab 2 is decreased for all the relevant frequencies as the velocity increases. Particularly, the reduction is significant at higher velocities and at lower angular frequencies. This explains the greater reduction of the magnitude of the peak at $\omega = 1.9 \times 10^{13} \text{ rad/s}$ compared to that at $\omega = 3.8 \times 10^{13} \text{ rad/s}$ as the velocity increases. For the modes with $q_x < 0$, the observer in the rest frame sees the exponentially suppressed number of thermal photons from slab 2 due to the motion-induced red-shift of the angular frequency. As a result, the net transferred number of thermal photons from slab 1 to slab 2 is increased as shown in Fig. 3(c). As the velocity increases, the drag force component on slab 2 due to the surface modes at around $\omega = 4.6 \times 10^{13} \text{ rad/s}$ increases. Overall, the increasing velocity of slab 2 results in a greater drag force component on it due to the Doppler shift of the angular frequency. The total force on slab 2 becomes zero at the velocity $V \approx 1.4 \times 10^3 \text{ m/s}$ at which the propulsion force due to the nonreciprocity and the increasing drag force due to the Doppler shift balances.

We numerically observed that the velocity dependence of the radiative heat flux and shear stress is dominated by the exponential change in the thermal occupation number. Then, the expansion of $n_B(\omega', T')$ with respect to velocity while setting $V = 0$ in τ leads to compact expressions of the radiative heat flux and the shear stress. The radiative heat flux and the shear stress can be expressed to the linear order in the nonrelativistic limit $\gamma = 1$ as

$$\varphi_{1 \rightarrow 2}(V) \approx \varphi_{1 \rightarrow 2}^0 - aV, \quad f_{x,2}(V) \approx f_{x,2}^0 - bV \quad (12)$$

where $\varphi_{1 \rightarrow 2}^0 \equiv \varphi_{1 \rightarrow 2}(V = 0)$ and $f_{x,2}^0 \equiv f_{x,2}(V = 0)$. The coefficients a and b are given as

$$\begin{aligned} \begin{bmatrix} a \\ b \end{bmatrix} &= \int_0^\infty \frac{d\omega}{2\pi} \int \frac{d\mathbf{q}}{(2\pi)^2} \hbar \begin{bmatrix} \omega \\ q_x \end{bmatrix} \frac{\hbar q_x}{k_B T_2} n_B(\omega, T_2') \\ &\times [n_B(\omega, T_2') + 1] \tau_{1 \rightarrow 2}(\omega, \mathbf{q}; V = 0). \end{aligned} \quad (13)$$

The derivation of Eq. (13) assumes that there is no velocity dependence of the transmission coefficient. The black dashed lines in Fig. 2(a) show the radiative heat flux calculated by the linear approximation in Eq. (12). The results agree very well with the full calculation up to a velocity $V \approx 5 \times 10^3$ m/s, which is beyond the steady-state velocity. The linear approximation of the shear stress also agrees well with the full calculation as shown in Fig. 2(b). In [37], the coefficients a and b are obtained in the operator form by generalizing the linear response expressions of the radiative heat and shear stress to the velocity of relative motion [44] for nonreciprocal systems. Moreover, the coefficient b is derived in the linear polarization basis in the electrostatic limit. Furthermore, the Onsager theorem for fluctuational electrodynamics [44] was used to show that the efficiency is bounded by the Carnot efficiency as far as small perturbations of velocity and temperature difference from the thermodynamic equilibrium are concerned. Here, we provide the linear response expressions in the linear polarization basis and show that they agree well with the full calculations. By taking the electrostatic limit in Eq. (13), the coefficient b should be identical to the friction coefficient in [37]. Furthermore, the expressions Eq. (12) can be applied to two objects at different temperatures.

The linear expansion of the radiative heat flux and shear stress reveals the competing effects that lead to the maximum thermodynamic efficiency seen in Fig. 2(c). Using Eq. (12),

this efficiency can be approximated up to the order of V^2 as

$$\eta \approx \frac{(f_{x,2}^0 - bV)V}{\varphi_{1 \rightarrow 2}^0 - aV} \approx \frac{f_{x,2}^0}{\varphi_{1 \rightarrow 2}^0} V - \frac{b}{\varphi_{1 \rightarrow 2}^0} V^2 + \frac{f_{x,2}^0 a}{(\varphi_{1 \rightarrow 2}^0)^2} V^2. \quad (14)$$

For small velocities, the efficiency increases linearly with respect to the velocity driven by the propulsion force, $f_{x,2}^0$, due to the nonreciprocity of the slab materials. As the velocity increases, the drag force component due to the exponential change in the thermal emission from slab 2, i.e., bV , becomes significant, which reduces the efficiency. While the efficiency increases due to the decrease of the heat flux, the overall effects from the terms with the quadratic velocity dependence reduce the efficiency. As a result, the efficiency reaches the maximum at the velocity around

$$V \approx \frac{f_{x,2}^0}{2\left(b - \frac{f_{x,2}^0 a}{\varphi_{1 \rightarrow 2}^0}\right)}. \quad (15)$$

The black dashed lines in Fig. 2(c) show the thermodynamic efficiency calculated by Eq. (14) and show a good agreement with the full calculation. We note that while the linear approximation works very well in our heat engine, the full calculation beyond the linear order and the velocity dependence of the transmission coefficient is critical in the operation of the system as a heat pump at high velocities as we will show in the next section. Finally, we note that the nonzero linear scaling of the radiative heat with respect to the velocity can be considered as a signature of nonreciprocity. When the two slabs are made of reciprocal materials, we can show that, $\varphi_{1 \rightarrow 2} - \varphi_{1 \rightarrow 2}^0 \propto V^2$ (see SM [50]), in contrast to the linear scaling $\propto V$ as seen for the nonreciprocal systems.

For the two source temperatures $T_1 = 305$ K and $T_2' = 300$ K considered in this paper, the Carnot efficiency is $\eta_{\text{Carnot}} \approx 0.016$. The maximum efficiency shown in Fig. 2(c), i.e., $\eta = 8 \times 10^{-4}$, is about 5% of the Carnot limit. To understand the origin of the discrepancy between the two efficiencies, we derive an ideal scenario where the heat engine operates at Carnot efficiency. In our formalism, each frequency is independent. Then, the Carnot efficiency of the heat engine is achieved if and only if the heat engine achieves the Carnot efficiency for each frequency. Since the operating velocity of the heat engine is nonrelativistic, we assume $\gamma = 1$. Also, we fix the frequency to be $\omega = \omega_0 > 0$, and consider the monochromatic thermodynamic efficiency $\eta(\omega_0) = \frac{f_{x,2}(\omega_0)V}{\varphi_{1 \rightarrow 2}(\omega_0)}$ in the following argument.

By rewriting the integral over q_x only in the positive region, the radiative heat flux and the shear stress on slab 2 are expressed as

$$\varphi_{1 \rightarrow 2}(\omega_0) = \int_0^\infty \frac{dq_x}{2\pi} \hbar \omega_0 \left[\{n_B(\omega_0, T_1) - n_B(\omega_0 - q_x V, T_2')\} \tau(q_x) + \{n_B(\omega_0, T_1) - n_B(\omega_0 + q_x V, T_2')\} \tau(-q_x) \right], \quad (16)$$

$$f_{x,2}(\omega_0) = \int_0^\infty \frac{dq_x}{2\pi} \hbar q_x \left[\{n_B(\omega_0, T_1) - n_B(\omega_0 - q_x V, T_2')\} \tau(q_x) - \{n_B(\omega_0, T_1) - n_B(\omega_0 + q_x V, T_2')\} \tau(-q_x) \right], \quad (17)$$

where $\tau(q_x) = \int_{-\infty}^\infty \frac{dq_y}{2\pi} \tau(q_x, q_y; V)$ and we omit V from the argument to simplify the notation. Here we assume that slab 2

is allowed to move only along the x direction. This assumption appears in the Doppler shift of the angular frequency in the

occupation number. The waves with both positive and negative q_x contribute to heat transfer from slab 1 to slab 2, but the contribution to the shear stress on slab 2 from modes with negative q_x acts as a drag force and reduces the conversion efficiency. This can be seen in the sign difference in front of the second term in Eqs. (16) and (17), and since $n_B(\omega_0, T_1) > n_B(\omega_0 + q_x V, T_2')$ for $T_1 > T_2'$ in the nonrelativistic velocities. Thus, to achieve ideal conversion efficiency from heat to mechanical work, the contributions from modes with negative q_x should be suppressed, i.e., we should set $\tau(-q_x) \rightarrow 0$ to obtain the thermodynamic efficiency as

$$\eta(\omega_0) = \frac{\int_0^\infty \frac{dq_x}{2\pi} q_x V [n_B(\omega_0, T_1) - n_B(\omega_0 - q_x V, T_2')] \tau(q_x)}{\int_0^\infty \frac{dq_x}{2\pi} \omega_0 [n_B(\omega_0, T_1) - n_B(\omega_0 - q_x V, T_2')] \tau(q_x)}. \quad (18)$$

To achieve the Carnot efficiency, we assume that for the angular frequency ω_0 , only modes with single q_{x0} are supported. In this case, Eq. (18) simplifies to

$$\eta(\omega_0) = \frac{q_{x0} V}{\omega_0}. \quad (19)$$

Thus, the efficiency linearly increases with V . The critical velocity V_c where the system reaches steady state can be obtained by setting $n_B(\omega_0, T_1) = n_B(\omega_0 - q_{x0} V, T_2')$, which results in

$$V_c = \frac{\omega_0}{q_{x0}} \left(1 - \frac{T_2'}{T_1}\right). \quad (20)$$

As $V \rightarrow V_c$, the heat engine approaches the Carnot efficiency $\eta(\omega_0) \rightarrow 1 - T_2'/T_1$. Note, however, that the power output approaches zero as the velocity reaches the critical velocity as expected for a Carnot engine.

In the derivation above we show how to achieve Carnot efficiency from heat transfer at a single frequency ω_0 . To achieve the Carnot efficiency over a broad range of frequencies, the critical velocity V_c as determined in Eq. (20) must be independent of ω_0 . Thus, the required dispersion is

$$\omega = \frac{V_c}{1 - \frac{T_2'}{T_1}} q_x, \quad \text{with } q_x > 0 \quad (21)$$

and no waves in the opposite direction $q_x < 0$. Thus, the discrepancy between the achievable efficiency in using n -InSb shown in Fig. 2(c) and the Carnot limit can be translated to the deviation of the supported modes, e.g., as in Fig. 3(b) for $\mathbf{q} = (q_x, 0)$, from the ideal dispersion in Eq. (21).

IV. HEAT PUMP

In the operation of the heat engine, the velocity of relative motion eventually reaches a steady state at which the output work is zero. In this section, we consider the situation where external work is applied on slab 2 to further increase the velocity beyond the steady-state velocity. In this case, the external work provides energy input to the system by operating against the drag force. As the velocity increases, the thermal emission from slab 2 is enhanced, which results in enhanced energy transfer from slab 2 to slab 1. At sufficiently high velocity, we show that the radiative heat flows from slab 2 at a lower proper temperature to slab 1 at a higher proper temperature. Hence, the system operates as a photonic heat pump that

utilizes external mechanical work to pump from a lower- to a higher-temperature object.

We consider the system under external work as shown in Fig. 1(b). We first provide an intuitive explanation of the mechanism of the photonic heat pump by considering an electromagnetic mode with ω and $\mathbf{q} = (q_x, 0)$. When slab 2 is moving at the relative velocity V in the positive x direction, the net radiative heat flux from slab 1 to slab 2 due to the modes with $q_x > 0$ satisfies $\varphi_{1 \rightarrow 2}(q_x) \propto \hbar \omega [n_B(\omega, T_1) - n_B(\gamma(\omega - q_x V), T_2')] \tau(q_x; V)$. As we discussed in the previous section, the increasing velocity of slab 2 induces the exponential enhancement of the thermal emission due to this mode from slab 2 for the observer in the rest frame. When the velocity is sufficiently high, the net radiative heat flux from these modes flows from slab 2 to slab 1 even when $T_1 > T_2'$ and hence $\varphi_{1 \rightarrow 2}(q_x) < 0$. The electromagnetic modes that contribute to cooling must have $n_B(\omega, T_1) < n_B(\gamma(\omega - q_x V), T_2')$, and thus must have the dispersion relation satisfying the constraint

$$\omega < \frac{V}{1 - \frac{T_2'}{\gamma T_1}} q_x \approx c \frac{T_1}{T_1 - T_2'} \frac{V}{c} q_x. \quad (22)$$

For nonrelativistic velocities, the constraint in Eq. (22) implies that $\omega \ll c q_x$ and thus requires a dispersion relation that lies outside the light cone. Therefore, the near-field radiative heat transfer is critical in order to achieve the heat pump.

For the modes with $q_x < 0$, the radiative heat flux is $\varphi_{1 \rightarrow 2}(-|q_x|) \propto \hbar \omega [n_B(\omega, T_1) - n_B(\gamma(\omega + |q_x| V), T_2')] \times \tau(-|q_x|; V)$. When $T_1 > T_2'$, these modes contribute to heating only. Therefore, to achieve cooling after integrating contributions from all modes, it is also required that the transmission coefficient exhibits strong enough nonreciprocity $\tau(q_x; V) \gg \tau(-q_x; V)$.

Based on the discussion above, two conditions are required to achieve cooling at nonrelativistic velocities. First, two slabs must support the electromagnetic modes whose dispersions satisfy the constraints of Eq. (22). This can be achieved by the coupled surface modes in the near field. Second, considering that the total radiative heat flux is integral over the frequency and wave-vector spaces, the surface modes that satisfy the dispersion Eq. (22), which contribute to cooling, must dominate over the other modes that contribute to heating. This is achieved by the nonreciprocity that allows strong directional surface modes.

Figure 4(a) and 4(b) show the radiative heat flux from slab 1 to slab 2 and the shear stress on slab 2, respectively, for the same materials and temperatures as the heat engine in Fig. 2, but in a range of higher velocity. The shear stress on slab 2 is negative and external work needs to be applied in order to move slab 2 at such velocities. In the absence of the external magnetic field, the radiative heat flux becomes negative for the velocity greater than 10^5 m/s, where the heat flows from slab 2 at a lower proper temperature to slab 1 at a higher proper temperature. This shows that structures made of reciprocal material can operate as a heat pump due to the nonreciprocal wave propagations as induced by the Doppler effect. With reciprocal materials, the heat pump cannot occur at nonrelativistic velocities if the velocity dependence of the transmission coefficient is ignored because the heating from

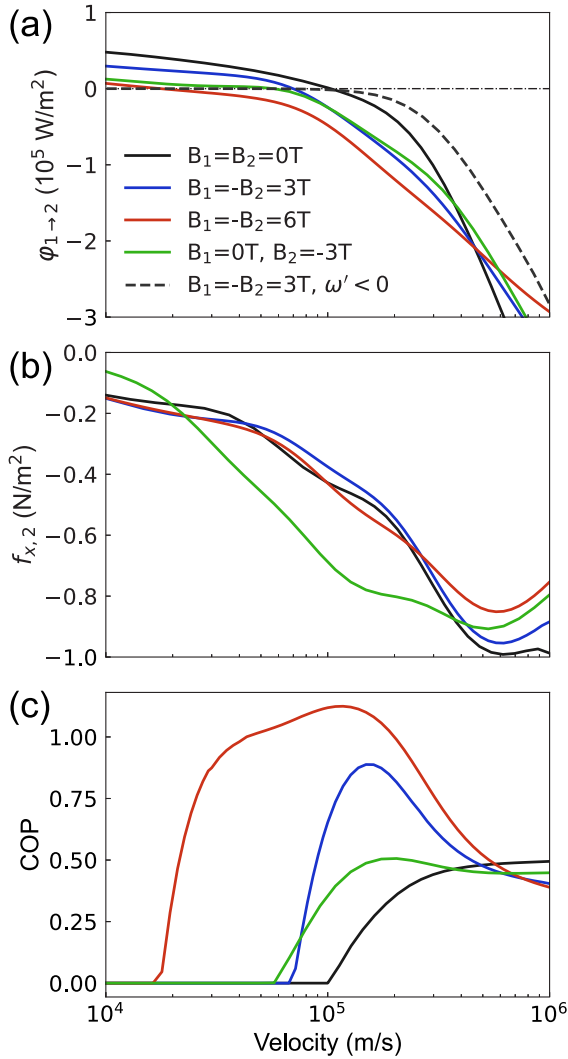


FIG. 4. (a) Radiative heat flux from slab 1 to slab 2, (b) shear stress on slab 2, and (c) coefficient of performance of the heat pump as a function of the velocity of relative motion. The physical parameters are the same as those in Fig. 2. The dash-dotted line in panel (a) describes $\varphi_{1 \rightarrow 2} = 0$. The COP is only defined for the region of $\varphi_{1 \rightarrow 2} < 0$ where the system operates as the heat pump. The black dashed line in panel (a) represents the radiative heat flux from the modes with $\omega' < 0$ only.

the modes with $q_x > 0$ always overcomes the cooling from the modes with $q_x < 0$. Hence, the velocity dependence of the transmission coefficient is essential in the heat pump regime when reciprocal materials are used. The application of the external static magnetic fields can lower the velocity at which the cooling occurs; with the presence of antiparallel magnetic fields of 6 T, the onset of the cooling occurs at a velocity of $V \approx 2 \times 10^4$ m/s, which is almost an order of magnitude lower as compared with that without the magnetic fields. Comparing the cases of $B_1 = B_2 = 0$ T and $B_1 = -B_2 = 3$ T, the greater amount of radiative heat can be pumped by applying less amount of external mechanical work when the velocity is below $V = 4.5 \times 10^5$ m/s. This shows that the nonreciprocal materials can enhance the performance of the heat pump. The magnitude of pumped radiative heat further

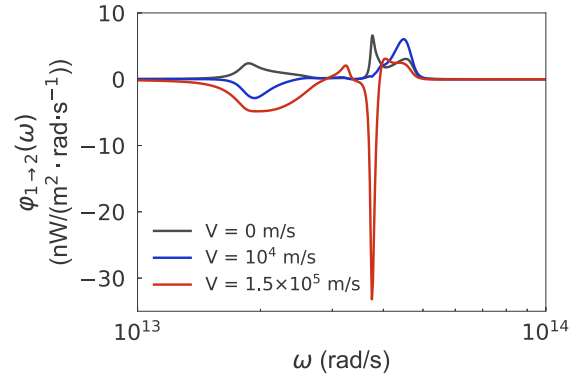


FIG. 5. Spectral radiative heat flux between two slabs under antiparallel static magnetic fields of 3 T for different velocities of relative motion. The other physical parameters are the same as those in Fig. 2.

increases under $B_1 = -B_2 = 6$ T while the shear stress exhibits a moderate change compared to the cases of $B_1 = B_2 = 0$ T and $B_1 = -B_2 = 3$ T. As a result, the heat pump performance further increases with increasing magnetic fields. Figure 4(c) shows the COP defined in Eq. (9). The onset of the heat pump operation at lower velocities and the enhancement of the performance by the external magnetic fields can be clearly seen.

Figure 5 shows the spectral radiative heat flux for different velocities under the application of the antiparallel external magnetic fields of 3T. To understand the evolution of the spectral radiative heat flux as the velocity increases, Figs. 6(a) and 6(b) show the transmission coefficients and Figs. 6(c) and 6(d) show the spectral radiative heat flux for the modes with $q = (q_x, 0)$ and for the two different velocities in the case of $B_1 = -B_2 = 3$ T. For other modes with nonzero q_y , the qualitative characteristics of the transmission coefficient are similar (see SM [50]). As discussed in Sec. II, the increase of the velocity reduces the net radiative heat flux from slab 1 to slab 2 due to the exponential change of the emission from slab 2. For the waves with dispersions that satisfy the constraint in Eq. (22), the exponential enhancement of thermal emission from slab 2 exceeds the thermal emission from slab 1, resulting in the net negative radiative heat flux and contributing to cooling. In Figs. 6(c) and 6(d), the right-hand side of Eq. (22) is plotted as the “cooling line.” Any mode that lies below the cooling line contributes to cooling. As shown in Fig. 6(c), at $V = 10^4$ m/s, the large part of the coupled surface plasmon modes around $\omega = 1.9 \times 10^{13}$ rad/s, which has $q_x > 0$ and $q_y = 0$, lies below the cooling line. Moreover, there are no surface modes near this frequency with $q_x < 0$ due to nonreciprocity. Thus, there is a significant contribution to cooling from these modes at $q_y = 0$. For the other waves with nonzero q_y , the net contribution to cooling is smaller due to the smaller portion of the surface waves that contribute to cooling. But the net cooling contribution persists after integrating over all q_y . As a result, the radiative heat flux at around $\omega = 1.9 \times 10^{13}$ rad/s is net negative as shown in Fig. 5. For the coupled surface phonon polariton modes at around $\omega = 3.8 \times 10^{13}$ rad/s, the cooling line intersects with its dispersion relation. Thus, the magnitudes of their contributions to heating and cooling

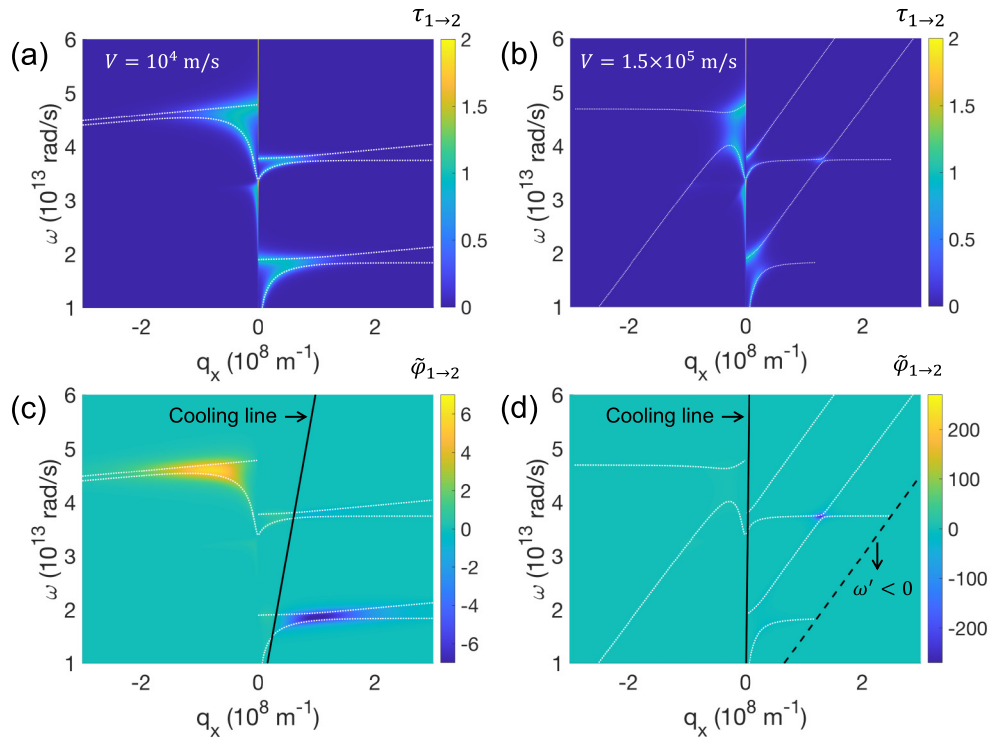


FIG. 6. (a, b) Plot of the transmission coefficient τ as a function of the frequency ω and x component of the wave vector q_x at $V = 10^4$ and 1.5×10^5 m/s, respectively. (c, d) Plot of mode-resolved radiative heat flux $\tilde{\varphi}_{1 \rightarrow 2}(\omega, q_x, q_y = 0)$ defined in the caption of Fig. 3. The unit is $[10^{-15} \frac{\text{W}\cdot\text{s}}{\text{rad}}]$. The physical parameters are the same as those in Fig. 2. The black lines in panels (c) and (d) are the constraint for cooling in Eq. (22). The dashed line in panel (d) is the line below which the angular frequency in the comoving frame is negative, i.e., $\omega' < 0$. The white dashed lines are the solutions of the dispersion relation Eq. (23) in the lossless limit.

are similar, resulting in the small radiative heat flux at $V = 10^4$ m/s as shown in Fig. 5. The coupled surface plasmon modes at around $\omega = 4.6 \times 10^{13}$ rad/s mostly have $q_x < 0$. Thus, the net radiative heat flux from slab 1 to slab 2 is enhanced due to the exponential suppression of thermal emission from slab 2. As a result, the spectral radiative heat flux increases at $V = 10^4$ m/s compared to that at rest. At $V = 10^4$ m/s, while the spectral radiative heat flux at the lower frequencies contributes to cooling, the overall radiative heat flux still flows from slab 1 to slab 2. However, the magnitude of radiative heat flux from slab 1 to slab 2 at $V = 10^4$ m/s is suppressed to almost half of that at rest.

As the velocity of relative motion further increases to $V = 1.5 \times 10^5$ m/s at which the COP reaches the maximum, the magnitude of the negative radiative heat flux from the modes below the cooling line further increases as shown in Fig. 6(d). At this velocity, the negative radiative heat flux dominates over the positive radiative heat flux even after integrating over the frequency and wave-vector space, which results in the heat pump as discussed in Fig. 4(a). Furthermore, Fig. 6(d) shows that the dominant contribution to cooling arises from the coupling between the surface plasmon and surface phonon polariton modes at around $\omega = 3.8 \times 10^{13}$ rad/s and $q_x = 2 \times 10^8$ m $^{-1}$ due to the Doppler shift of the surface plasmon modes, which will be discussed in detail below. The contribution from this coupled mode appears as a strong peak in Fig. 5.

Another observation from Fig. 6 is the strong modification of the dispersion relation of the surface modes compared with the case of $V = 0$ shown in Figs. 3(b) and 3(d). In Fig. 6(d), the dispersion of the surface waves for $q_x > 0$ and $q_x < 0$ shows upward and downward tilting, respectively, due mostly to the Doppler shift of the angular frequency. Suppose that the resonance condition of a surface wave on slab 1 is satisfied in the rest frame, i.e., for a given q_x , $\omega = f(q_x)$, where f is the dispersion of the surface wave. In the comoving frame, the same surface mode is supported on the surface of slab 2, i.e., $\omega' = f(q'_x)$. When observing this surface wave from the rest frame, the Lorentz transformation of the frequency and wave vector results in the surface wave supported at the interface of the moving slab as $\omega \approx q_x V + f(q_x)$. Thus, the dispersion curve shows upward or downward tilting by $q_x V$ depending on the sign of q_x . The Lorentz transformation of the frequency is the effect of Doppler shift. This Doppler shift of the angular frequency results in the off resonance of the two surface waves that are in resonance at rest. The decoupling of the surface waves typically causes a smaller transmission coefficient at the original resonant frequency and instead the transmission coefficient spreads over a wider frequency range around the original resonant frequency. Interestingly, the opposite can happen at high velocities. At high velocities, two surface modes supported on two slabs that are off resonance in the absence of the relative motion can be brought into resonance in the presence of the relative motion. To show this clearly, the

dispersion of the surface waves supported between the two slabs at relative motion with nonrelativistic velocities is derived (see SM [50] for derivation) for the Voigt configuration [57] where the wave vector $\mathbf{q} = (q_x, 0)$ is perpendicular to the magnetic field as

$$\begin{aligned} & \left[-\frac{\omega'}{\omega} + \frac{1}{\varepsilon_V^{(1)} \varepsilon_V^{(2)}} \left(\frac{\varepsilon_{xz}^{(2)}}{\varepsilon_{xx}^{(2)}} \frac{q_x}{k_z} + i \frac{\kappa_2'}{k_z} \right) \left(\frac{\varepsilon_{xz}^{(1)}}{\varepsilon_{xx}^{(1)}} \frac{q_x}{k_z} - i \frac{\kappa_1}{k_z} \right) \right] \\ & \times \tanh(-ik_z d) - \frac{1}{\varepsilon_V^{(2)}} \left(\frac{\varepsilon_{xz}^{(2)}}{\varepsilon_{xx}^{(2)}} \frac{q_x}{k_z} + i \frac{\kappa_2'}{k_z} \right) \\ & + \frac{\omega'}{\omega} \frac{1}{\varepsilon_V^{(1)}} \left(\frac{\varepsilon_{xz}^{(1)}}{\varepsilon_{xx}^{(1)}} \frac{q_x}{k_z} - i \frac{\kappa_1}{k_z} \right) = 0, \end{aligned} \quad (23)$$

where $\kappa_1 = \sqrt{q_x^2 - \varepsilon_V^{(1)} k_0^2}$, $\kappa_2' = \sqrt{q_x^2 - \varepsilon_V^{(2)} k_0'^2}$, $k_z = \sqrt{k_0^2 - q_x^2}$, and $\varepsilon_V^{(i)} = \varepsilon_{zz}^{(i)} + (\varepsilon_{xz}^{(i)})^2 / \varepsilon_{xx}^{(i)}$, $i = 1, 2$ where the subscripts stand for the elements of the dielectric function tensor. For slab 2, the dielectric functions are evaluated in the comoving frame, i.e., $\varepsilon_{zz}^{(2)} = \varepsilon_{zz}^{(2)}(\omega')$, $\varepsilon_{xz}^{(2)} = \varepsilon_{xz}^{(2)}(\omega')$. The solutions of Eq. (23) in the lossless limit are plotted in Fig. 6 by the white dotted lines for the region where $\omega' > 0$. The dispersion relation Eq. (23) reproduces the velocity dependence of the surface waves by the full calculations very well. In Fig. 6(d), the dispersion curve Eq. (23) clearly shows that the surface plasmon modes that are blue-shifted due to the Doppler effect come into resonance with the surface phonon polariton modes at around $\omega = 3.8 \times 10^{13}$ rad/s. Although the transmission coefficient as a result of the resonance is moderate, i.e., $\tau \approx 0.15$, the modes are supported at the high in-plane momentum. As a result, the contribution to the radiative heat flux becomes significant as we discussed in Fig. 5. Note however that such modes are supported at the high in-plane momentum, and the incorporation of nonlocal effects into our dielectric function models can suppress the resonance. Nevertheless, this result shows that the Doppler shift can provide an additional control knob to engineer two off-resonant modes into resonance. We also note that the photonic heat pump can occur without this coincidental resonance. In fact, the heat pump can be achieved by magnetized plasma by turning off the contribution from the phonon polaritons, i.e., $\varepsilon_{\text{ph}} = 0$ (see SM [50]).

Finally, we emphasize that the heat pump does not require electromagnetic modes with negative frequencies in the comoving frame, i.e., $\omega' < 0$. In such regimes, from the viewpoint of the observer in the rest frame, the moving slab behaves as a gain material. In general, the modes with $\omega' < 0$ contribute to the cooling since $n_B(\omega', T_2') \tau_{1 \rightarrow 2} > 0$. The black dashed line in Fig. 6(d) sets the boundary below which the frequency in the comoving frame becomes negative. One can see that all relevant electromagnetic modes contributing to the heat pump exist in the positive frequency domain. However, as the relative velocity increases further the significant contribution comes from the modes with negative frequencies in the comoving frame. The contribution of the modes with $\omega' < 0$ to the radiative heat flux under the antiparallel magnetic fields of 3 T is shown in Fig. 4(a). At $V = 1.5 \times 10^5$ m/s where the maximum COP is achieved, the contribution from the negative frequency modes is less than 10% of the total radiative heat flux and even less at lower velocities. Thus, those modes

are not required to achieve the heat pump. As the velocity increases, the contribution to the radiative heat flux from the modes with $\omega' < 0$ becomes dominant.

V. RELATIVISTIC THERMODYNAMIC EFFICIENCY

The thermodynamic efficiency of the heat engine considered in this paper is defined as Eq. (9). For situations where the velocity of relative motion is nonrelativistic, i.e., $\gamma \approx 1$, we showed that such definition of the thermodynamic efficiency of the heat engine approaches the Carnot efficiency $1 - \frac{T_2'}{T_1}$ when the electromagnetic modes satisfy the dispersion in Eq. (21). In principle, we can conceive of a heat engine where two slabs are in relative motion at relativistic velocities. For such systems, as we will show below, the efficiency as defined in Eq. (9) is problematic. For the observer in the rest frame, this definition leads to the efficiency limit of $1 - \frac{T_2'}{\gamma T_1}$. On the other hand, for the observer in the comoving frame, it leads to the limit of $1 - \frac{\gamma T_2'}{T_1}$. Therefore, this definition results in the thermodynamic limit that depends on the frame of reference. This indicates that in some inertial frame, the efficiency limit is higher than what one may define as the sensible definition of the Carnot efficiency $1 - \frac{T_2'}{T_1}$. Moreover, in the limit of $V \rightarrow c$, it indicates that the perfect conversion of heat into work is possible in the rest frame since $\gamma \rightarrow \infty$.

The difficulty of the efficiency definition in Eq. (9) originates from the definition of $f_{x,2} V$ as the useful work in our system, which does not take the relativity effects into account. It was pointed out that with different choices of the forms of useful work, the relativistic Carnot efficiency in the rest frame can take different forms $\eta = 1 - \frac{\gamma^a T_2'}{T_1}$ where $a = 0, \pm 1$ [58]. Thus, the problem is also closely related to the Lorentz transformation of the temperature of the moving material $T_2 = T_2' \gamma^a$ where T_2 is the temperature of the moving material in the rest frame, which has been a topic of discussion for decades and remains to be answered [59].

In this section, our purpose is to derive the expression of relativistic thermodynamic efficiency for our system that considers the relativistic effects. We focus on the operation of the system as a heat engine to derive the relativistic thermodynamic efficiency, but a similar argument should follow for the operation as a heat pump. First, we show that the efficiency bound based on the nonrelativistic thermodynamic expression Eq. (9) depends on the frame of reference in the relativistic regime. Adopting the viewpoint of Landsberg and Johns [58] that the Carnot limit should not depend on the choice of a particular reference frame, we discuss two contributions as nonextractable work by using the relativistic thermodynamics [60]. By considering these contributions to the definition of useful work, we derive the relativistic thermodynamic efficiency and show that it is bounded by the Carnot efficiency which is independent of the frame of reference.

First, we can prove the following identity (see detailed derivation in SM [50]):

$$T_1 f_{x,2} V \leq \left| T_1 - \frac{T_2'}{\gamma} \right| \text{sgn} \left(T_1 - \frac{T_2'}{\gamma} \right) \varphi_{1 \rightarrow 2}. \quad (24)$$

By applying Eq. (24) to the expressions of the conventional thermodynamic efficiency of Eq. (9), we can find the

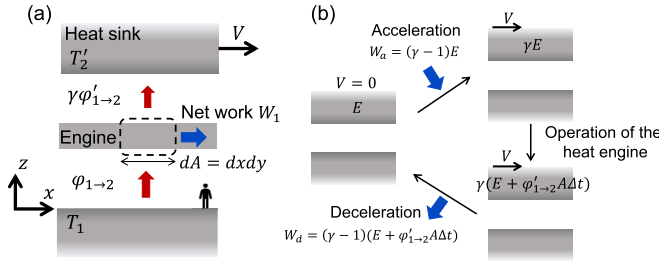


FIG. 7. (a) Application of the first law of relativistic thermodynamics on the control volume enclosed by the dashed line. slab 2 is hypothetically separated into the engine and heat sink, both of which are moving at the velocity V . (b) The evolution of the energy of slab 2 and the work done to slab 2 for acceleration W_a and the work extracted by decelerating slab 2 W_d . For both panels, we consider the observer is in the rest frame with slab 1.

efficiency bound as

$$\eta = \begin{cases} \frac{f_{x,2}V}{\hat{\varphi}_{1 \rightarrow 2}} \leq 1 - \frac{T'_2}{\gamma T_1} & \text{if } T_1 > \frac{T'_2}{\gamma} \\ \frac{f_{x,2}V}{\hat{\varphi}_{1 \rightarrow 2} + f_{x,2}V} \leq 1 - \frac{\gamma T_1}{T'_2} & \text{if } T_1 < \frac{T'_2}{\gamma} \end{cases}, \quad (25)$$

where $\hat{\varphi}_{1 \rightarrow 2} = \text{sgn}(T_1 - \frac{T'_2}{\gamma})\varphi_{1 \rightarrow 2}$ and this definition is meaningful only if $f_{x,2}V \geq 0$. Thus, the conventional thermodynamic efficiency expression in Eq. (25) leads to the bound that depends on the frame of reference due to the dependence on the Lorentz factor γ .

The contribution that cannot be extracted as useful work originates from the change of momentum of slab 2 as a result of heat transfer. In relativistic mechanics, the changes of energy and momentum are directly related. In the rest frame, the x component of the momentum of a moving body at the velocity V in the x direction is related to its energy E by $G_x = \frac{E}{c^2}V$. To identify the part of work that is nonextractable, we separate slab 2 into a hypothetical engine connected to an infinitely large heat sink at T'_2 . Both the hypothetical engine as well as the heat sink move at the velocity V as shown in Fig. 7(a). We consider the control volume with the surface area $dA = dx dy$ on the xy plane that encloses the engine. For this control volume, we consider the first law of relativistic thermodynamics from the viewpoint of an observer in the rest frame [60]:

$$dE = \delta Q + \delta W + V dG_x. \quad (26)$$

This relativistic first law of thermodynamics dictates that the energy change dE of the control volume is due to the heat input to the control volume, δQ , the work done to the control volume, δW , and the change of the momentum associated with the heat transferred to the control volume, $V dG_x$. We apply Eq. (26) to one cycle of the heat engine and we denote the period as Δt . The heat transferred to the control volume is $\frac{\delta Q}{A \Delta t} = \varphi_{1 \rightarrow 2}$ where A is a surface area of the control volume measured in the rest frame. The work done to the control volume is $\frac{\delta W}{A \Delta t} = -f_{x,2}V$. The contribution to the energy change due to the change of the momentum is $\frac{V dG_x}{A \Delta t} = \beta^2 \frac{dE}{A \Delta t}$. In the operation of a heat engine, the system must return to the same thermodynamic state as the initial state after one cycle. In relativistic thermodynamics, it means that the system must

retain not only the same energy but also the same momentum after one cycle. Thus, in order to keep the momentum of the moving medium unchanged after one cycle, the amount $\beta^2 \frac{dE}{A \Delta t}$ has to be rejected to the heat sink and cannot be used as useful work. The energy change of the control volume after one cycle is given from Eq. (26) as

$$\frac{dE}{A \Delta t} = \gamma^2 (\varphi_{1 \rightarrow 2} - f_{x,2}V) = \gamma \varphi'_{1 \rightarrow 2}. \quad (27)$$

Subtracting the nonextractable work $\beta^2 \frac{dE}{A \Delta t}$ from $f_{x,2}V$, we have the net useful work from the engine as

$$W_1 = f_{x,2}V - \gamma^2 \beta^2 (\varphi_{1 \rightarrow 2} - f_{x,2}V). \quad (28)$$

Another way to interpret Eq. (28) is that the total energy change in the control volume after one cycle must be zero. Thus, the amount of energy given in Eq. (27) must flow into the heat sink to keep the momentum unchanged. Then, the useful work is given as $W_1 = \varphi_{1 \rightarrow 2} - \gamma \varphi'_{1 \rightarrow 2}$, which is the same result as Eq. (28).

The other missing contribution in Eq. (25) is the additional work that can be extracted as a result of the energy increase of slab 2 after one cycle. Consider the operation of the heat engine from the state where the two slabs are at rest. To operate the heat engine at finite velocity V , we need work to accelerate slab 2. In our heat engine, this work is provided by the propulsion force driven by the nonequilibrium lateral Casimir force. After the operation of the heat engine at the velocity V , we decelerate slab 2 until the two slabs are at rest. Under the adiabatic approximation for the acceleration and deceleration, the amount of work required for the two processes is given as the differences in the kinetic energies. In nonrelativistic physics, the works required for the two processes are the same because the mass of slab 2 is invariant before and after the operation of the heat engine. However, in the relativistic cases, the work done by slab 2 in the deceleration is greater than the work done to slab 2 to accelerate due to the energy increase of slab 2 after the acceleration process. In principle, this difference between the two can be extracted as useful work.

To estimate the portion of the work, we consider operating the heat engine from the slabs at rest and determine the amount of work necessary to accelerate slab 2 to the velocity at which we operate the heat engine and decelerate it back to rest after the operation of the heat engine as shown in Fig. 7(b). We consider the adiabatic acceleration and deceleration of slab 2 from the point of the observer in the rest frame. Then, the work required to accelerate slab 2 to the velocity V is given by the energy difference $W_a = (\gamma - 1)E$ where E is the energy of slab 2 at rest. During the operation of the heat engine over the time period Δt , the increase of the energy of slab 2 evaluated in the comoving frame is $\varphi'_{1 \rightarrow 2} A' \Delta t' = \varphi'_{1 \rightarrow 2} A \Delta t$ where we used $A \Delta t = A' \Delta t'$, which results from the fact that the number of photons is Lorentz invariant. Thus, the work that can be extracted by decelerating slab 2 to rest is given as $W_d = (\gamma - 1)(E + \varphi'_{1 \rightarrow 2} A \Delta t)$. This is greater than the work required for the acceleration process. Then, the net mechanical work that can be extracted is given as the difference between them as $W_d - W_a = (\gamma - 1)\varphi'_{1 \rightarrow 2} A \Delta t = \gamma(\gamma - 1)(\varphi_{1 \rightarrow 2} - f_{x,2}V)A \Delta t$ where we used Eq. (8). Thus, the portion of the work per unit area per cycle contributed by the

mechanical energy of slab 2 is given as

$$W_2 = \gamma(\gamma - 1)(\varphi_{1 \rightarrow 2} - f_{x,2}V), \quad (29)$$

which needs to be added to the useful work.

Overall, the amount of useful work per unit area per second is

$$W_{\text{net}} = W_1 + W_2 = f_{x,2}V - \gamma^2\beta^2(\varphi_{1 \rightarrow 2} - f_{x,2}V) + \gamma(\gamma - 1)(\varphi_{1 \rightarrow 2} - f_{x,2}V). \quad (30)$$

And the relativistic thermodynamic efficiency for $T_1 > \frac{T'_2}{\gamma}$ is given as

$$\eta_{\text{rel}} = \frac{W_{\text{net}}}{\varphi_{1 \rightarrow 2}} = \frac{\gamma f_{x,2}V - (\gamma - 1)\varphi_{1 \rightarrow 2}}{\varphi_{1 \rightarrow 2}}. \quad (31)$$

In the nonrelativistic limit, Eq. (31) goes back to the conventional nonrelativistic thermodynamic efficiency. By using the efficiency bound Eq. (25), we find that the relativistic thermodynamic efficiency is bounded by the Carnot efficiency that is independent of the frame of reference:

$$\eta_{\text{rel}} \leq 1 - \frac{T'_2}{T_1}. \quad (32)$$

The appreciable difference between the relativistic thermodynamic efficiency and the nonrelativistic one is observed when the velocity of relative motion is a sizable fraction of the speed of light.

VI. CONCLUSIONS

In summary, we studied a system consisting of two semi-infinite parallel slabs with different temperatures as a photonic heat engine driven by nonequilibrium lateral Casimir forces. To analyze the system, we formulated the radiative heat flux and shear stress between two nonmagnetic slabs with general dielectric function tensors that are moving relative to each other at arbitrary velocities. For the photonic heat engine to self-start, one of the materials must break Lorentz reciprocity and we considered n-InSb under static external magnetic fields. The Doppler effect of the angular frequency causes the exponential change of the thermal photon number emitted

from the moving slab as the velocity increases. We revealed that such exponential change plays the essential role for the moving slab to reach the steady-state velocity. This insight leads to the linear approximation of the radiative heat flux and shear stress that agreed well with the full calculations. Furthermore, we showed the ideal frequency dispersion with which the photonic heat engine achieves Carnot efficiency requires truly one-way propagations.

We also showed that this system operates as a photonic heat pump if a sufficiently high velocity of relative motion is realized by external work. We showed that a photonic heat pump does not require external magnetic fields due to nonreciprocal wave propagations induced by the relative motion. Nevertheless, the use of nonreciprocal materials by the application of static external magnetic fields can further reduce the required velocity of relative motion and enhance the performance of the heat pump. Our calculations indicated that the dispersion relation of the surface modes is strongly altered at high velocities of relative motion and brings two off-resonant surface modes at rest into resonance in the presence of relative motion. Finally, we considered operating the heat engine at relativistic velocities and derived the relativistic thermodynamic efficiency of the photonic heat engine and pump. We showed that the efficiency is bounded by the Carnot efficiency that is independent of the frame of reference. Regarding the experimental feasibility of our system, Srituravanich *et al.* demonstrated a flying plasmonic lens at a speed of 12 m/s with a distance of 20 nm away from a surface [61]. In our paper, we have assumed a speed that is about two orders of magnitude higher. Further optimization of the dispersion relation of the slab structures may lead to a lower speed requirement.

Our results point to a way of thermal energy harvesting and cooling by nonequilibrium Casimir forces enabled by breaking Lorentz reciprocity.

ACKNOWLEDGMENTS

This work is supported by a MURI program from the U.S. Army Research Office (Grant No. W911NF-19-1-0279). We thank Dr. Mohammed Benzaouia for a fruitful discussion.

-
- [1] E. G. Cravalho, C. L. Tien, and R. P. Caren, Effect of small spacings on radiative transfer between two dielectrics, *J. Heat Transfer* **89**, 351 (1967).
 - [2] C. M. Hargreaves, Anomalous radiative transfer between closely-spaced bodies, *Phys. Lett. A* **30**, 491 (1969).
 - [3] D. Polder and M. Van Hove, Theory of radiative heat transfer between closely spaced bodies, *Phys. Rev. B* **4**, 3303 (1971).
 - [4] J.-P. Mulet, K. Joulain, R. Carminati, and J.-J. Greffet, Nanoscale radiative heat transfer between a small particle and a plane surface, *Appl. Phys. Lett.* **78**, 2931 (2001).
 - [5] J.-P. Mulet, K. Joulain, R. Carminati, and J.-J. Greffet, Enhanced radiative heat transfer at nanometric distances, *Microscale Thermophys. Eng.* **6**, 209 (2002).
 - [6] S. Shen, A. Narayanaswamy, and G. Chen, Surface phonon polaritons mediated energy transfer between nanoscale gaps, *Nano Lett.* **9**, 2909 (2009).
 - [7] E. Rousseau, A. Siria, G. Jourdan, S. Volz, F. Comin, J. Chevrier, and J.-J. Greffet, Radiative heat transfer at the nanoscale, *Nat. Photonics* **3**, 514 (2009).
 - [8] R. S. Ottens, V. Quetschke, S. Wise, A. A. Alemi, R. Lundock, G. Mueller, D. H. Reitze, D. B. Tanner, and B. F. Whiting, Near-Field Radiative Heat Transfer between Macroscopic Planar Surfaces, *Phys. Rev. Lett.* **107**, 014301 (2011).
 - [9] T. Kralik, P. Hanzelka, V. Musilova, A. Srnka, and M. Zbac, Cryogenic apparatus for study of near-field heat transfer, *Rev. Sci. Instrum.* **82**, 055106 (2011).

- [10] K. Kim, B. Song, V. Fernández-Hurtado, W. Lee, W. Jeong, L. Cui, D. Thompson, J. Feist, M. T. H. Reid, F. J. García-Vidal *et al.*, Radiative heat transfer in the extreme near field, *Nature (London)* **528**, 387 (2015).
- [11] H. B. G. Casimir, On the attraction between two perfectly conducting plates, *Proc. Kon. Ned. Akad. Wet.* **51**, 793 (1948).
- [12] H. B. G. Casimir and D. Polder, The influence of retardation on the London–van der Waals forces, *Phys. Rev.* **73**, 360 (1948).
- [13] E. M. Lifshitz, The theory of molecular attractive forces between solids, *Sov. Phys.* **2**, 73 (1956).
- [14] S. K. Lamoreaux, Demonstration of the Casimir Force in the 0.6 to 6 μm Range, *Phys. Rev. Lett.* **78**, 5 (1997).
- [15] U. Mohideen and A. Roy, Precision Measurement of the Casimir Force from 0.1 to 0.9 μm , *Phys. Rev. Lett.* **81**, 4549 (1998).
- [16] C. Henkel, K. Joulain, J. P. Mulet, and J. J. Greffet, Radiation forces on small particles in thermal near fields, *J. Opt. A Pure Appl. Opt.* **4**, S109 (2002).
- [17] M. Antezza, L. P. Pitaevskii, and S. Stringari, New Asymptotic Behavior of the Surface-Atom Force out of Thermal Equilibrium, *Phys. Rev. Lett.* **95**, 113202 (2005).
- [18] M. Antezza, L. P. Pitaevskii, S. Stringari, and V. B. Svetovoy, Casimir-Lifshitz Force Out of Thermal Equilibrium and Asymptotic Nonadditivity, *Phys. Rev. Lett.* **97**, 223203 (2006).
- [19] M. Antezza, L. P. Pitaevskii, S. Stringari, and V. B. Svetovoy, Casimir-Lifshitz force out of thermal equilibrium, *Phys. Rev. A* **77**, 022901 (2008).
- [20] A. O. Sushkov, W. J. Kim, D. A. R. Dalvit, and S. K. Lamoreaux, Observation of the thermal Casimir force, *Nat. Phys.* **7**, 230 (2011).
- [21] J. L. Pan, H. K. H. Choy, and C. G. Fonstad, Very large radiative transfer over small distances from a black body for thermophotovoltaic applications, *IEEE Trans. Electron Devices* **47**, 241 (2000).
- [22] R. S. DiMatteo, P. Greiff, S. L. Finberg, K. A. Young-Waithe, H. K. H. Choy, M. M. Masaki, and C. G. Fonstad, Enhanced photogeneration of carriers in a semiconductor via coupling across a nonisothermal nanoscale vacuum gap, *Appl. Phys. Lett.* **79**, 1894 (2001).
- [23] A. Narayanaswamy and G. Chen, Surface modes for near field thermophotovoltaics, *Appl. Phys. Lett.* **82**, 3544 (2003).
- [24] J. Fang, H. Frederich, and L. Pilon, Harvesting nanoscale thermal radiation using pyroelectric materials, *J. Heat Transfer* **132**, 092701 (2010).
- [25] A. Fiorino, L. Zhu, D. Thompson, R. Mittapally, P. Reddy, and E. Meyhofer, Nanogap near-field thermophotovoltaics, *Nat. Nanotechnol.* **13**, 806 (2018).
- [26] F. Capasso, J. N. Munday, D. Iannuzzi, and H. B. Chan, Casimir forces and quantum electrodynamical torques: Physics and nanomechanics, *IEEE J. Sel. Top. Quantum Electron.* **13**, 400 (2007).
- [27] T. Emig, Casimir-Force-Driven Ratchets, *Phys. Rev. Lett.* **98**, 160801 (2007).
- [28] A. Ashourvan, M. Miri, and R. Golestanian, Noncontact Rack and Pinion Powered by the Lateral Casimir Force, *Phys. Rev. Lett.* **98**, 140801 (2007).
- [29] R. Zhao, L. Li, S. Yang, W. Bao, Y. Xia, P. Ashby, Y. Wang, and X. Zhang, Stable Casimir equilibria and quantum trapping, *Science* **364**, 984 (2019).
- [30] M. G. Silveirinha, S. A. H. Gangaraj, G. W. Hanson, and M. Antezza, Fluctuation-induced forces on an atom near a photonic topological material, *Phys. Rev. A* **97**, 022509 (2018).
- [31] S. A. Hassani Gangaraj, G. W. Hanson, M. Antezza, and M. G. Silveirinha, Spontaneous lateral atomic recoil force close to a photonic topological material, *Phys. Rev. B* **97**, 201108(R) (2018).
- [32] D. Pan, H. Xu, and F. J. García de Abajo, Magnetically activated rotational vacuum friction, *Phys. Rev. A* **99**, 062509 (2019).
- [33] M. F. Maghrebi, A. V. Gorshkov, and J. D. Sau, Fluctuation-Induced Torque on a Topological Insulator out of Thermal Equilibrium, *Phys. Rev. Lett.* **123**, 055901 (2019).
- [34] C. Khandekar and Z. Jacob, Thermal spin photonics in the near-field of nonreciprocal media, *New J. Phys.* **21**, 103030 (2019).
- [35] C. Khandekar, S. Buddhiraju, P. R. Wilkinson, J. K. Gimzewski, A. W. Rodriguez, C. Chase, and S. Fan, Nonequilibrium lateral force and torque by thermally excited nonreciprocal surface electromagnetic waves, *Phys. Rev. B* **104**, 245433 (2021).
- [36] Y. Guo and S. Fan, Single gyrotropic particle as a heat engine, *ACS Photonics* **8**, 1623 (2021).
- [37] D. Gelbwaser-Klimovsky, N. Graham, M. Kardar, and M. Krüger, Near Field Propulsion Forces from Nonreciprocal Media, *Phys. Rev. Lett.* **126**, 170401 (2021).
- [38] R. Golestanian and M. Kardar, Path-integral approach to the dynamic Casimir effect with fluctuating boundaries, *Phys. Rev. A* **58**, 1713 (1998).
- [39] T. Emig, A. Hanke, R. Golestanian, and M. Kardar, Probing the Strong Boundary Shape Dependence of the Casimir Force, *Phys. Rev. Lett.* **87**, 260402 (2001).
- [40] F. Chen, U. Mohideen, G. L. Klimchitskaya, and V. M. Mostepanenko, Demonstration of the Lateral Casimir Force, *Phys. Rev. Lett.* **88**, 101801 (2002).
- [41] A. Manjavacas, F. J. Rodríguez-Fortuño, F. J. García de Abajo, and A. V. Zayats, Lateral Casimir Force on a Rotating Particle near a Planar Surface, *Phys. Rev. Lett.* **118**, 133605 (2017).
- [42] B. Müller and M. Krüger, Anisotropic particles near surfaces: Propulsion force and friction, *Phys. Rev. A* **93**, 032511 (2016).
- [43] M. Reid, O. Miller, A. Polimeridis, A. Rodriguez, E. Tomlinson, and S. Johnson, Photon torpedoes and Rytov pinwheels: Integral-equation modeling of non-equilibrium fluctuation-induced forces and torques on nanoparticles, [arXiv:1708.01985](https://arxiv.org/abs/1708.01985).
- [44] V. A. Golyk, M. Krüger, and M. Kardar, Linear response relations in fluctuational electrodynamics, *Phys. Rev. B* **88**, 155117 (2013).
- [45] S. M. Rytov, Y. A. Kravtsov, and V. Tatarskii, *Principles of Statistical Radiophysics* (Springer, Berlin, 1989).
- [46] S. A. Biehs, P. Ben-Abdallah, F. S. S. Rosa, K. Joulain, and J. J. Greffet, Nanoscale heat flux between nanoporous materials, *Opt. Express* **19**, A1088 (2011).
- [47] L. Fan, Y. Guo, G. T. Papadakis, B. Zhao, Z. Zhao, S. Buddhiraju, M. Orenstein, and S. Fan, Nonreciprocal radiative heat transfer between two planar bodies, *Phys. Rev. B* **101**, 085407 (2020).
- [48] A. I. Volokitin and B. N. J. Persson, Near-field radiative heat transfer and noncontact friction, *Rev. Mod. Phys.* **79**, 1291 (2007).
- [49] A. I. Volokitin and B. N. J. Persson, Theory of the interaction forces and the radiative heat transfer between moving bodies, *Phys. Rev. B* **78**, 155437 (2008).

- [50] See Supplemental Material at <http://link.aps.org/supplemental/10.1103/PhysRevB.107.115406> for detailed derivations of the formalism in this paper.
- [51] J. D. Jackson, *Classical Electrodynamics* (American Association of Physics Teachers, 1999).
- [52] M. Fizeau, Sur les hypothèses relatives à l'éther lumineux, et sur une expérience qui paraît démontrer que le mouvement des corps change la vitesse avec laquelle la lumière se propage dans leur intérieur, *CR Hebd. Avad. Sci.* **33**, 349 (1851).
- [53] R. Fleury, D. L. Sounas, C. F. Sieck, M. R. Haberman, and A. Alù, Sound isolation and giant linear nonreciprocity in a compact acoustic circulator, *Science* **343**, 516 (2014).
- [54] S. Maayani, R. Dahan, Y. Kligerman, E. Moses, A. U. Hassan, H. Jing, F. Nori, D. N. Christodoulides, and T. Carmon, Flying couplers above spinning resonators generate irreversible refraction, *Nature (London)* **558**, 569 (2018).
- [55] E. Moncada-Villa, V. Fernández-Hurtado, F. J. García-Vidal, A. García-Martín, and J. C. Cuevas, Magnetic field control of near-field radiative heat transfer and the realization of highly tunable hyperbolic thermal emitters, *Phys. Rev. B* **92**, 125418 (2015).
- [56] E. D. Palik, *Handbook of Optical Constants of Solids* (Academic, New York, 1985).
- [57] K. W. Chiu and J. J. Quinn, Magneto-plasma surface waves in solids, *II Nuovo Cimento B (1971-1996)* **10**, 1 (1972).
- [58] P. T. Landsberg and K. A. Johns, Carnot efficiencies for moving reservoirs, *J. Phys. A Gen. Phys.* **5**, 1433 (1972).
- [59] C. Farías, V. A. Pinto, and P. S. Moya, What is the temperature of a moving body? *Sci. Rep.* **7**, 17657 (2017).
- [60] R. C. Tolman, *Relativity, Thermodynamics, and Cosmology* (Courier, New York, 1987).
- [61] W. Srituravanich, L. Pan, Y. Wang, C. Sun, D. B. Bogy, and X. Zhang, Flying plasmonic lens in the near field for high-speed nanolithography, *Nat. Nanotechnol.* **3**, 733 (2008).